In Situ tensile tests to analyze the mechanical response, crack initiation, and crack propagation in single polyamide 66 fibers

Alba Marcellan, Anthony Bunsell, Roland Piques, Lucien Laiarinandrasana

To cite this version:

Alba Marcellan, Anthony Bunsell, Roland Piques, Lucien Laiarinandrasana. In Situ tensile tests to analyze the mechanical response, crack initiation, and crack propagation in single polyamide 66 fibers. Journal of Polymer Science Part B: Polymer Physics, 2019, 57 (11), pp.680-690. 10.1002/polb.24823 . hal-02486413

HAL Id: hal-02486413
https://hal.science/hal-02486413v1

In Situ Tensile Tests to Analyse the Mechanical Response, Crack Initiation and Crack Propagation in Single Polyamide 66 Fibres.

Alba Marcellan[1], Anthony Bunsell[2], Roland Piques[2], Lucien Laiarinandrasana[2]

[1]Soft Matter Sciences and Engineering, ESPCI Paris, PSL Research University, Sorbonne University, CNRS, F-75005 Paris, France

[2]PSL-Research University, MINES ParisTech, PSL Research University, CNRS UMR7633, BP 87, F-91003 Evry Cedex, France

Correspondence to: Alba Marcellan (e-mail: alba.marcellan@espci.fr)

(Additional Supporting Information may be found in the online version of this article.)

ABSTRACT

Single fibre mechanical testing is challenging to perform, especially when the diameter is as small as tens of micrometres. For this reason, real time observations of crack propagation mechanisms have been rarely been investigated experimentally. This paper presents experimental and numerical investigations of fracture of monofilamentary high performance polyamide 66 fibres. Their engineering stress-strain curves are compared. The mechanisms of failure starting from crack initiation until the final brittle fracture are studied by *in situ* tests in Scanning Electron and optical microscopes. Finite element modelling at the individual fibre scale has been performed in 3D, as a reverse engineering method. The compliance method was used to determine the crack depth that triggers the final failure. The fracture toughness was numerically determined using the *J-integral* concept, accounting for the geometry of the crack front (3D) together with plastic deformation. 3D meshes were designed especially from *post-mortem* observations. The average value deduced was about (47 ± 7) kJ.m^{-2}, which will be discussed with other estimates using linear elastic fracture mechanics.

KEYWORDS: fracture, crack propagation, polymer, fibre

INTRODUCTION

High performance fibres are designed to face industrial challenges for materials that demand high resistance and lightness. Fibres offer technical solutions in many technological fields, particularly for composite engineering or the design of technical textiles. Two aspects make fibres quite remarkable materials. First, by inducing a highly oriented structure, this is especially the case for polymers, a great enhancement of the specific modulus along the fibre axis can be achieved compared to unoriented materials[1-3]. The second feature is the high aspect ratio of the structure: a fibre diameter is typically tens of micrometres, with monofilaments for particular uses having diameters up to hundreds of microns, whereas fibre lengths can be up to several meters or virtually continuous, depending on applications. Thus, despite high tensile moduli, fibres as elementary mechanical structures are highly flexible and can easily be organized into complex multi-assemblies like yarns or fabrics.[4-6] In that context, the single fibre undergoes multi-axial mechanical loadings together with complex fibre-fibre frictional contacts[7].

From a fundamental point of view, as for all materials, the mechanical properties of the single fibre can be classified into two categories:
1. The constitutive relationship in general, that is the function relating the stress and strain and specifically the stiffness (Young's modulus);
2. The failure characteristics (stress or strain at break, the fracture toughness).

For many bulk materials, a current framework of research deals with the link between the evolution of microstructure under stress and both its mechanical stiffness and toughness, for instance in polyamide 6 (PA6).[8,9] Likewise for fibres, although the mechanical characterization at the single fibre scale is challenging, especially when the diameter is as small as tens of micrometres, identifying the micro-mechanisms involved in the mechanical responses at the single fibre scale (along the fibre axis and in the perpendicular direction) remains crucial.

For the first category of mechanical property – the stiffness – attention has to be paid to the relevant microstructural details able to track the mechanisms of deformation at the scale of the fibre. Thus, our previous work on Polyamide 66 fibres demonstrated that besides the effect of crystalline domains (amount and orientation), the fraction of oriented amorphous phase in the fibre appeared also to be good criteria for predicting mechanical stiffness.[10] As in most studies on this subject, focus was given to the change of the microstructure related to the level of deformation in the longitudinal direction using the engineering stress-strain curve. Transverse mechanical properties of fibres have received even less attention due to the aforementioned difficulties related to their fineness.[3]

Regarding failure properties of polymer fibres, single fibre stress (and strain) at break often remain the gold-standards as quantitative descriptors of ultimate properties.[11,12] Yet, often neither stress nor strain at break can provide a satisfactory failure criterion due to the lack of knowledge on the distributions of defects, their nature and sizes. Thus, a comprehensive analysis of fracture based on failure strength requires a very large number of tests allowing a probabilistic failure analysis.[13]

So far, the fracture mechanisms underlying the failure of the polymer fibre have been deduced from post-mortem fracture surface examinations. This has been pioneered by Hearle *et* al.[14] with the advent of scanning electron microscopy. Since then extensive observations have been made of fibre fracture surfaces to try to reveal the failure processes involved (fractography) of numerous kinds of textile.[15-17]

More recent developments were made in the field of inorganic fibres. Rolland *et al.*[18] using *in situ* tomography analysed the mechanisms of fibre failure in a glass fibre reinforced composite subjected to cyclic loading. The examinations of the fracture surfaces of broken glass fibres during fatigue tests led the authors to estimate the fracture toughness of the glass fibres using linear fracture mechanics. Naito *et al.*[19] systematically observed the fracture surfaces of broken carbon fibres from single fibres tested in tension and identified similar fracture patterns independently of the gauge length. Other recent pioneer works have used the Focused Ion Beam (FIB) technique so as to introduce a notch at single fibre scale on brittle fibres[20-25] such as silicon carbide, carbon fibres, etc. This single edge notched tensile (SENT) like geometry allowed the fracture toughness of these fibres to be determined with a 2D or 3D approach.

Whatever the goal of these studies, often, *post-mortem* observations by scanning electron microscopy (SEM) have remained the only tool to infer the fracture mechanisms. But linking the fracture surface aspects to the mechanisms of failure might be problematic without a real time detailed knowledge of the mechanisms of failure. Indeed, the fracture surface is the state of the material after experiencing highly non-linear phenomena such as the stress/strain singularity at the crack tip, the high viscous and plastic deformations and complex micro-damage in the process zone.

Similar to the difficulties relating microstructural evolution of polymer fibres to the tensile stress-strain curve, the real time observation of crack propagation mechanisms have been rarely investigated experimentally.[26,27]

In this paper, an attempt has been made to characterize comprehensive mechanical properties of single Polyamide 66 (PA66) fibres, using both experimental and numerical approaches. The materials under study will first be presented, followed by a detailed description of the experimental setup used to perform *in situ* tensile tests on smooth and pre-cracked single fibres. The results will then be presented in terms of experimental data associated with numerical simulations by a fully 3D finite element analysis. This latter method has allowed a successful simulation of the crack growth at the fibre scale. This enabled the determination of fracture toughness: the critical energy release rate at the onset of the final brittle failure.

EXPERIMENTAL AND NUMERICAL METHODS

Materials

Commercial yarns of PA 66 have been studied. Two of them were high performance and ultra-high performance multifilaments, respectively labelled as HP and UHP, both used for tyre reinforcement. A third type of PA66 fibre, specifically a "large diameter" MonoFilament (with a mean diameter of 200 µm), denoted as MF, was used to support the crack initiation and propagation investigations. Indeed, without the FIB technique, a larger diameter was required to overcome the experimental difficulty related to the implantation of a pre-crack and optical observations of the fracture mechanisms at the single fibre scale.

TABLE 1 Nomenclature and technical specifications of the PA66 fibres

Fibre	*UHP*	*HP*	*MF*
Filament	multifilament		mono
Linear density	7.5 dtex*	7.5 dtex*	360 dtex*
Diameter	29 µm	29 µm	200 µm
Number of fibres /yarn	280	280	1

*1 dtex is equivalent to the mass (in g) of 10,000 m of yarn

Tensile tests on smooth and pre-cracked single fibres

The dimensions of the fibres required special testing techniques to ensure the measurement in the appropriate range of stiffness. Single fibre tensile tests were performed using the universal fibre tester developed in the laboratory, the details of which have been given elsewhere.[10]

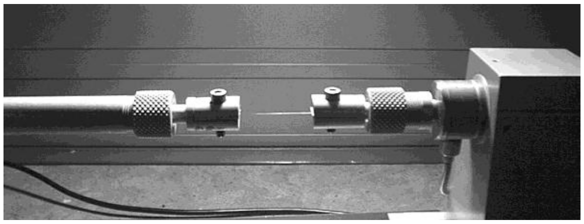

FIGURE 1. Design of the single fibre tensile machine.

As shown in Figure 1, the fibre was held horizontally between two clamps, one was fixed and the other was connected to a movable cross-head supplied with a load cell. The gauge length was fixed at 50 mm. The displacement of the cross-head was controlled by a LVDT transducer. The resolution of the load and the displacement were respectively 0.1 g (Sensotec load cell of 2.5 N) and 0.01% (LVDT sensor from Sensotec). The tests were conducted at 21°C and 50% relative humidity and at a nominal strain rate of $1.6\ 10^{-2}\ s^{-1}$. Fibre diameters were systematically measured before tests with an accuracy of 0.1 µm.

In situ tests have been performed in the chamber of a Scanning Electron Microscope (SEM) to examine the change in the microstructure at the surface during the tensile test. These observations for small diameter fibres were carried out using a LEO 1450VP SEM equipped with a micro-tensile machine. The specimen gauge length was about 2 mm. Many attempts were made to select pre-existing defects within this gauge length, but they were not those which provoked the final failure of the sample. The results presented here concerned the unique sample that allowed the evolution of the fibre around the defect to be clearly analysed during the tensile test. Unfortunately, the design of the micro-tensometer did not enable recordings of the displacement or the load. However, the images obtained, although not synchronized with any mechanical quantity, allowed a better understanding of the deformation, damage and failure mechanisms at the surface during a tensile test.

To proceed further with the understanding of the mechanisms of crack initiation and growth, pre-cracked MF fibres were also tested. Conversely to the FIB technique, the initial notch was made by hand, using a razor blade. The tensile test was instrumented with a long distance microscope using a typical magnification of about 450X (QM1, Questar). Therefore, the load versus crack opening displacement curve was recorded in real time, mimicking a fracture mechanics test on a single edge notch tensile (SENT) specimen.

Finally, *post-mortem* observations of the fibre fracture surfaces (Au-Pd coated for metallization) were performed using a LEO DSM982 Gemini Field Emission Gun Scanning Electron Microscope at an acceleration voltage of 2 kV. These examinations were systematically carried out on initially notched or un-notched fibres.

Finite element (FE) modelling

Fracture mechanics tests on the MF fibres were simulated using an *in-house* finite element code: Zset® suite computing solution (http://zset-software.com/). The Zset optimizer routine was used to obtain a set of material coefficients using data from single fibres (here on MF). The crack growth in 3D was then simulated using “release nodal degree of freedom” numerical technique.[28] The purpose was to validate the set of material parameters in the model and to determine the crack depth that triggered the final brittle failure of the fibre. The energy release rate from a 3D mesh was computed so as to determine the fracture toughness of the material.

RESULTS AND DISCUSSION

Mechanical response under monotonic longitudinal loading

A morphological study was first carried out, focusing on the cross-section of an embedded bundle of fibres. Fibre cross-section analysis (SEM images) confirmed the cross-section circularity of the fibres and enabled the mean diameter to be measured. As shown in Figure 1, the longitudinal response was characterized by monotonic tensile tests on single fibres. Typical engineering stress strain curves are represented in the Figure 2. The stress-strain curves represent a representative curve over at least 30 tests performed under the conditions described above. The general response in the tensile mode was relatively similar for all the PA66 fibres tested.

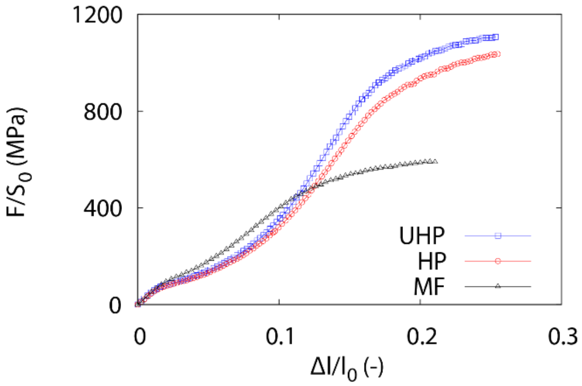

FIGURE 2. Tensile responses of different grades of PA66 fibres.

As expected from previous studies on PA66 fibres [10,13,29,30] the tensile response exhibited strong non-linearity with three main regions. Typically, below 2% of strain, the initial part of the curve exhibited a quasi-linear stress-strain dependency. Indeed, results gave a quite similar initial longitudinal Young moduli E, ranging from 5.0 to 5.3 GPa for the three grades of fibres. Up to a strain of about 0.02, curves were concave upwards due to a progressive alignment of the macromolecules upon loading.[10] The last deformation regime revealed a plateau domain in which the tangent moduli were rather low. For comparison purposes, it has been noted that up to 0.1 engineering strain, fibre MF had the highest stiffness followed by UHP and HP fibres. Beyond this, the stress-strain curve underwent a final decline that led to failure. The HP and UHP fibres revealed the same trends from about 0.14 engineering strain. The ultimate slopes of UHP and HP fibres were similar although the stresses/strains at failure were different. The viscoelastic effects were investigated over an order of magnitude variation of the strain rate and appeared quite negligible on the mechanical response.[10] Table 2 summarizes the specific initial Young's moduli, the ultimate strengths and the engineering strains at failure of the 3 tested fibres.

Table 2. Young's moduli obtained and mean properties at failure ($1.6\ 10^{-2}\ s^{-1}$).

Fibre	*UHP*	*HP*	*MF*
Modulus, *E* (GPa)	5.3 ± 0.2	4.8 ± 0.2	5.0 ± 0.2
Strength* (MPa)	1190 ± 60	929 ± 50	602 ± 15
Strain at failure*	0.25 ± 0.02	0.22 ± 0.02	0.19 ± 0.02

*Mean value over at least 30 tests per conditions to ensure statistical reproducibility.

In Figure 2, oscillations were observed in the plateau of the plot for UHP and HP. They were assumed to be due to micro-cracks consecutively initiating from ruptures of polymer macrofibrils observed at the surface of the fibres.[10]

This motivated *in situ* tests so as to analyse the evolution of the material around pre-existing defects when they initiated the failure mechanisms of the sample.

Observations during *in situ* tensile test

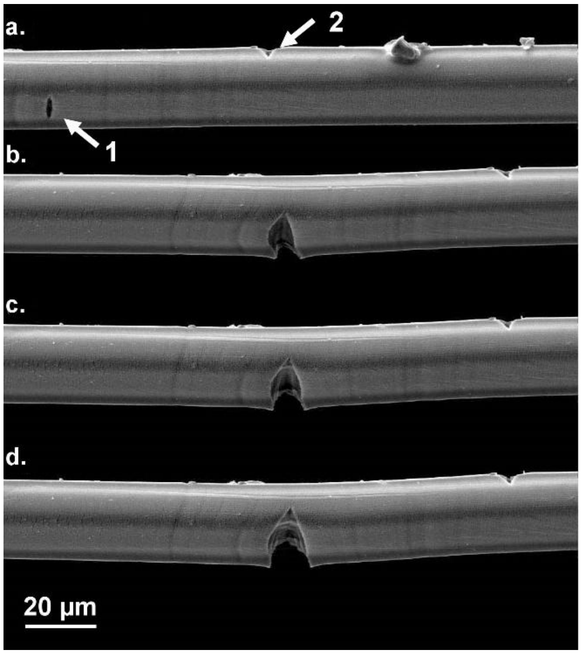

FIGURE 3. *In situ* tensile test on a single UHP fibre carried out in a SEM chamber. a, Two pre-existing defects, indicated by arrows (1) and (2) were observed. Several deformation ratios were applied before inducing crack opening (1), see b. For b, c and d, crack propagated at a constant applied strain. Elapsed time between each pictures was around 20 sec.

Figure 3 summarizes the deformation and fracture mechanisms observed during a tensile test in a SEM chamber on a 29 µm diameter PA66 fibre. As far as authors know, such observation in a 30 µm-fibre is unreported. Two pre-existing defects, indicated by arrows (1) and (2) were observed (Figure 3a). As mentioned above, such an *in situ* observation of the phenomenon is quite exceptional because of the randomness of crack initiation compared to the entire gauge length (approximately 2 mm). The tensile direction was horizontal, the left side of the fibre being blocked whereas the displacement was applied to the end of the monofilament on the right. Actually, the loading consisted of a short relaxation test where no measurement of the load/displacement was recorded. After 3 minutes no visible crack propagation was noticed. A series of increments of displacement was first applied, before any crack propagation became visible (from Figure 3a to Figure 3b). As can be observed, this produced the opening of defect 1 whereas the general morphology of defect 2 did not change. Next, the applied displacement was held constant. Crack propagation was then followed in real-time, with 20 sec intervals between images (from Figures 3b, 3c and 3d) caused by the time elapsed due to the electron beam scanning. The opening displacement as well as the depth of the initiated micro-crack continuously increased although the stress was supposed to relax (displacement held constant). It is to be noted that upon loading, some evidence of strain concentration along the fibre was highlighted by some flaking of the surface coating (metallization). This helped to localize these initial cracks.

Figure 3 displays side views from which the evolution of the crack opening displacement and the crack depth were clearly observed. An analysis of the facture surfaces by SEM was performed to complete the study.

Revisiting the fracture surfaces examinations

First, the fracture surfaces of fibres after monotonic tensile tests up to failure were examined, i.e., on un-notched fibres. Figure 4 shows the two fracture surfaces of UHP fibres related to a given tensile test. The other investigated PA66 grades featured the same pattern as expected from the literature.[16] The crack can be supposedly initiated at or near the fibre surface. Consecutively, two distinct fracture surface aspects – structure and geometry – were noticed. The first zone, called "sub-critical" shows an inclined surface with respect to the fibre axis due to the opening of the initiated crack. Some fibrils appear on the fracture surface. This inclined pattern could be assumed to be a ductile fracture surface.

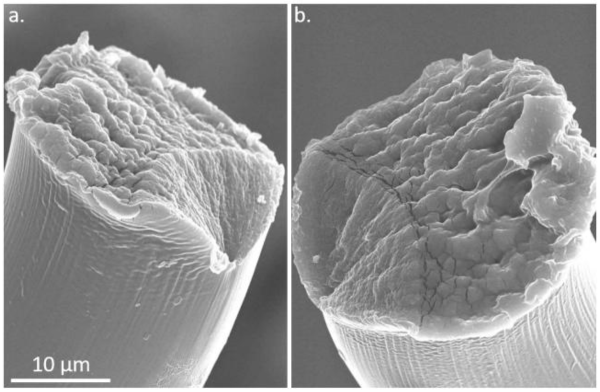

FIGURE 4. Complementary fracture surfaces of the UHP fibre broken in a monotonic tensile test.

The inclination comes from the blunting of the crack due to plastic deformation ahead of the crack, as can be seen in the side view on Figure 3b, corresponding to the loading stage. It is to be noted that Figures 4a and b show the complementary fracture surfaces from the same tensile test illustrating that the fractured morphology was symmetrical (cup-cup). This symmetry of the fracture pattern clearly indicates that the rupture occurs in an opening mode (Mode I). Moreover the crack front in this ductile part was curved as can be seen at the boundary of the two surface aspects.

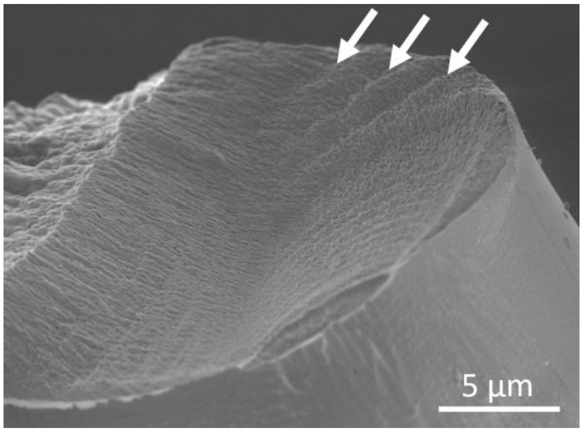

FIGURE 5. Fracture surfaces from broken specimen after an *in situ* test in a SEM chamber (see, Figure 3).

The second zone, attributed to rapid propagation, had a globular topology. The fracture surface was oriented perpendicularly to the axis of the fibre. This aspect was interpreted as showing a brittle surface pattern, corresponding to the ultimate mechanisms of failure.

Figure 5 details the fracture surface topology of the broken fibre where the crack was initiated from a defect 1 (see Figure 3). Two initiation sites seem to appear near the surface. The last part of the crack propagation (in the left of Figure 5) showed both the inclined ductile and the flat brittle fracture surfaces, respectively. With the help of the consecutive side views illustrated in Figure 3, the following chronology of the crack growth was determined:
- First “transverse” propagation occurred during the loading stage (Figure 3a) ;
- Then, the second step observed at the onset of the inclined surface exhibited steps or waves (see white arrows in Figure 5). This propagation by discontinuous bands is similar to that reported by Hamouda *et al.*[31] on slow crack growth of polyethylene subjected to creep tests. Here, it can then be attributed to the consecutive mini-relaxation tests (from Figure 3a to b).
- The final surface (inclined perpendicular to the fibre axis) corresponded to the final rapid failure which was too quick for any image of any further stage of propagation to be obtained. Note that the above mentioned fracture surface patterns (Figure 4) were observed independently to the applied strain rate.[10]

***In situ* tensile test on pre-cracked SENT MF fibres**

As mentioned above, a better understanding of the mechanisms of crack initiation and propagation was attempted using larger diameter PA66 fibres with a single edge notch, even though it must be accepted that texture at the molecular level could have been different. Michielsen[32] reported the possible influence of the gauge length-to-diameter ratio on the bending of the specimen during the tensile tests due to the asymmetry of the crack. The main objective of these tests was to provide complete experimental data to feed the FE simulations.

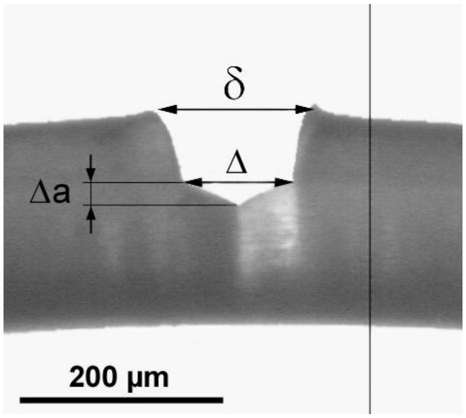

FIGURE 6. Characteristic lengths measured during the tensile test on pre-cracked MF fibre. Vertical line is due to the presence of a graticule on the objective.

Four *in situ* tensile tests were carried out with an optical microscope. The load and applied displacement were recorded whereas the crack opening displacement (COD) δ, and the crack tip opening displacement (CTOD) Δ and the crack advance Δa were synchronized with the load versus displacement using measurements taken from the pictures. The measurement of the characteristic lengths such as Δa,

δ, Δ in real time from side views is illustrated in Figure 6. The bending of the fibre sample can be seen from the curvature of the line opposite to the opening displacement δ. It was assumed that, as a more local measure, δ takes this bending effect into account, alleviating the dependency to the length-to-diameter ratio. Furthermore, a reverse shape of blunting crack tip was noticed. Indeed, the shape of the CTOD did not show the same curvature as common blunting of crack tip (convex instead of concave). It can be supposed to be attributed to the projection effects on the side view.

Figure 7 summarizes the experimental data results in which the load F (first Y axis) versus opening displacement together with the crack advance (second Y axis) have been plotted.

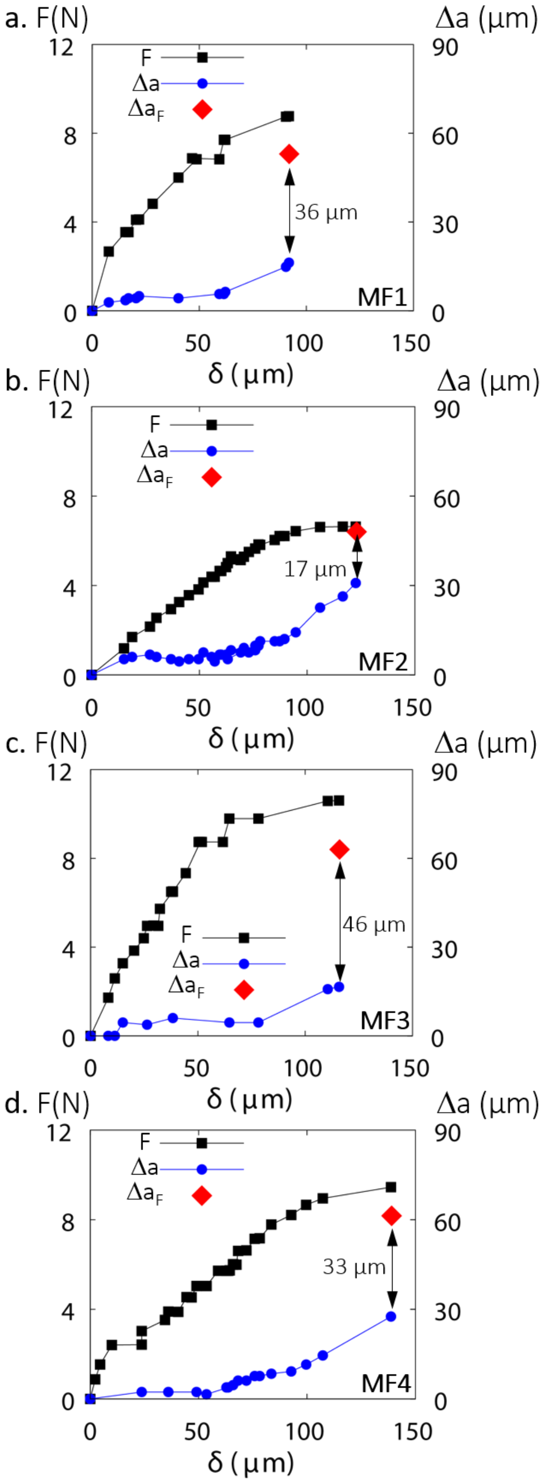

FIGURE 7. Typical experimental data obtained from the tensile tests on pre-cracked MF fibres. The crack advance Δa measured by *in situ* optical observations (until a maximal value a_{max}) is compared to Δa_F obtained by post-mortem SEM examination.

A lower confidence on the Δa measurement than that of the load should be mentioned. Indeed, a small twist angle or a small torsion of the fibre may alter the side view measurement. The crack advance measurement during *in situ* tests was therefore completed by top view SEM examinations of the fracture surfaces so as to analyse the shape and to estimate the real crack depth.

Figure 8 shows up these fracture surfaces from the four pre-cracked samples. Each fracture surface was composed of three surface aspects, similar to that reported by Michielsen.[32]
The first consisted of the mark of the initial notch produced by a razor blade. The surface was neat and the crack front at the end obviously straight. This was followed by an inclined surface similar to that of the ductile surface in the un-notched specimen. The crack front was curved with a peculiar curvature since the crack depth was smaller in the central part than at the surface. This is opposed to the so-called "tunnel effects" in common fracture mechanics specimens. Indeed, for cracked round bars the effects of crack shape (semi-elliptical or semi-circular) were studied with opposite curvature to that observed in Figure 8.[33]

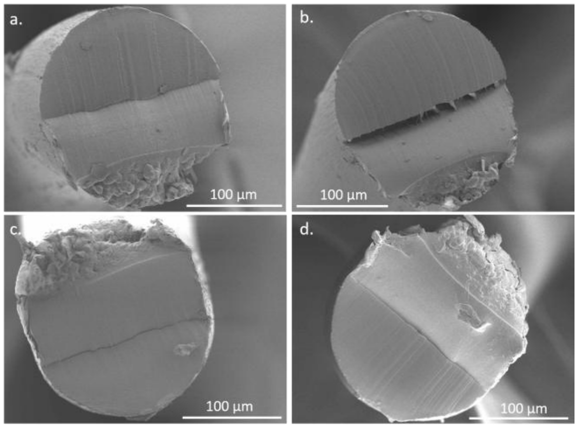

FIGURE 8. Typical fracture surfaces obtained from the tensile tests on pre-cracked MF fibres: (a) MF1, (b) MF2, (c) MF3, (d) MF4.

As this inclined surface can be supposed to be the zone where the convex blunting of the initial crack was located, three reasons might be considered to explain this shape, beyond the projection effects:
1. Possible skin-core effects like residual stresses already reported in previous work[3,13,29] ;
2. The bending effect due to the asymmetry of the crack in a SENT like geometry: the neutral fibre location due to this bending being different at the surface from that in the central part;
- The viscoelastic effect that may change the fracture surface aspects in the observed conditions, i.e., in the fully relaxed state (long-time elapsed after test).

The final surface is perpendicular to the direction of the loading similar to the brittle pattern corresponding to the rapid failure of the specimen. It can then be concluded that *in situ* tests on MF pre-cracked samples were able to reproduce the fracture surfaces of initially smooth specimens.

TABLE 3 Characteristic lengths for MF specimens

Fibre	*MF1*	*MF2*	*MF3*	*MF4*
a_0 (µm)	89	104	70	78
a_{max}(µm)	105	135	86	106
a_F (µm)	142	152	133	139
a* (µm)	137	-	113	131

Note that a_0 and a_F were measured *post-mortem* by SEM, a_{max} under *in situ* conditions by optical microscopy. a* was obtained by reverse engineering using FE methods.

From the fracture surface examinations shown in Figure 8, the initial and final crack depths (a_0 and a_F respectively) were measured. Table 3 shows these values together with a_{max}, the last crack depth measured during *in situ* tests from side views. It should be noted that a_{max} was systematically less than a_F. The gap between these two measurements is shown in Figure 7 plots where full diamonds in red (one point for each plot) represent a_F. The last blue full circle corresponded to a_{max}. These gaps were more than 30 µm apart from MF2 sample for which the initial crack depth was more than half of the section radius involving a complex interplay between mode I and in-plane shear (mode II) fracture mode. This can be observed in Figure 8b displaying crack bifurcation. Due to this specificity, MF2 specimen data were not considered in the following.

The large discrepancy observed between the *in situ* evaluation and the *post-mortem* measurement can be attributed to the difficulty of measuring the crack advance under *in situ* conditions. The measurement takes place on the surface of the fibre and the phenomena of perspective could induce a significant shift of the "true" quantities. In addition, the comparison of measurements made under *in situ* and *post-mortem* conditions – SEM micrographs – reveals differences in terms of loading conditions, as *post-mortem* morphologies are morphologies at rest.

Finite Element modelling

The load versus opening displacement curves were used to obtain the fracture toughness of the MF fibre. Theoretically, the fracture toughness is the energy release rate corresponding to the onset of the final brittle failure.[34] For common specimen geometries (Compact tension or Single Edge Notched Bending…), available energy release rate – and the corresponding stress intensity factor – formulae can be obtained, generally expressed in 2D (plane strain[20,33] or plane stress). For round bars containing central flaws, a table of stress intensity factors is given in Toribio *et al.*[33] where the material is supposed to have linear elastic behaviour. In the present study, as observed experimentally, the pseudo SENT round bars exhibited strong 3D effects (complex crack front) together with large plastic deformation, so that a finite element computation of the *J-integral* was carried out to evaluate the energy release rate, by benefitting from the crack propagation experimental data.[20,33,35] The fracture toughness J_{IC} was then considered as the value of the *J-integral* at the initiation of brittle failure.

To this end, an elasto-plastic model was selected for the large diameter fibre. For the smooth specimen, the optimized set of material coefficients allowed a comparison between the experimental and the simulated Cauchy stress (true stress) versus logarithmic strain (true strain) curve (Figure9).

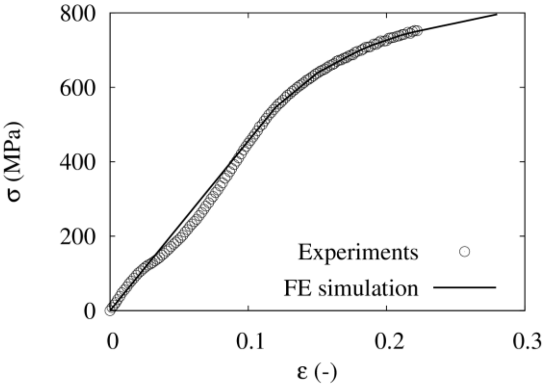

FIGURE 9. True stress-strain curve of MF fibre: experimental and FE simulation with the optimized set of material parameters.

It should be mentioned that a hyperelastic model was also tested so as to take the first inflexion (at $\varepsilon = 0.25$) of the curve into account. Since, the study focuses on the ultimate parameters of the material, this first inflexion was neglected. The hyperelastic model will not be further discussed.

Concerning the pre-cracked fibre, the fracture toughness should be calculated for a crack depth corresponding to the onset of the brittle failure. As mentioned in Table 3, the extreme crack depths measured *in situ* from side views a_{max}, were less than those measured from the *post-mortem* fracture surfaces by SEM. The purpose of the first part of the numerical simulation was then to determine the appropriate crack depths resulting in final brittle failure at the maximum load, using the compliance (inverse of the stiffness) method assisted by FE modelling. The compliance of the cracked specimen depends on the crack depth ratio. If the constitutive model is relevant, the FE simulated load versus δ curve should be in line with the experimental one by fixing the crack depth value. To this end, the remaining ligament was meshed for each of the geometries so as to make appear three crack depths, respectively a_0 , a_{max} and a_F (Table 3). For simplification purposes, the crack front was assumed to be straight. Figure 10 details the top views of the afore-mentioned 3D meshes.

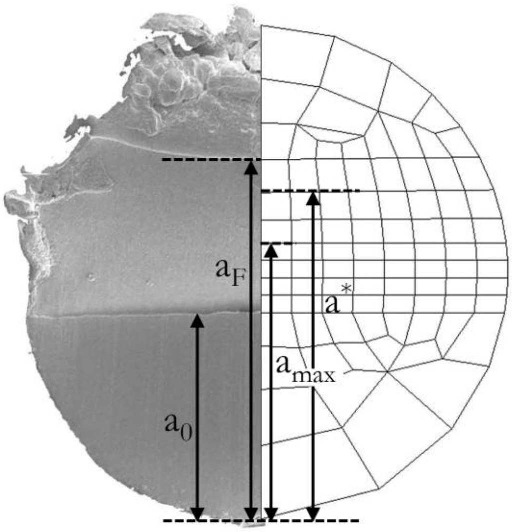

FIGURE 10. FE mesh of the remaining ligaments of MF fibres. This mesh corresponds to MF4 test. (Crack depths are defined in Table 3).

A first attempt was made to run FE computations with stationary cracks, i.e., without crack propagation, with three crack depths obtained from observations: a_0, a_{max} and a_F respectively (see Figure 11). It can be seen in Figure 11 that the deeper the crack, the greater the compliance of the specimen.[13] Except for MF4, the initial compliance (a_0) coincided with that of the experimental data whereas that corresponding to a_F was systematically overestimated. As shown in Figure 11, none of these stationary cracks satisfied the experimental compliance on the whole range of δ. It was then proceeded to optimize the crack depth value a^* within the interval [a_{max} and a_F] that allowed for the simulated and experimental F-δ curves to be in good agreement, especially the final compliance. The values of a^* obtained are shown in the last line of Table 3. The comparison between experimental data and simulated F-δ curves are illustrated in Figure 11. Excellent argument is clearly obtained apart from around the first inflexion.

To go further, FE simulations of propagating cracks were carried out using a release node technique.[28] This methodology does not intend to predict the fracture toughness of the material but deals with a numerical simulation of the crack propagation by imposing the history of the crack advance included in the experimental data from *in situ* tests.

The principle relied on the release of nodes located behind the remaining ligament. The degree of freedom of the element, along the axis of stress, was then relaxed. An optimization of the propagation of the crack, Δa versus δ, was carried out so that the numerical calculation fitted best the experimental compliance F-δ.

As observed in Figure 11, this approach allowed good agreement, between experimental data and the simulated load versus δ curve with evolving compliance (red open polygons), to be obtained, even around the first inflexion. Only the simulated curve of MF4 deviated from the experimental one. In the following this test will not be taken into account in the discussion.

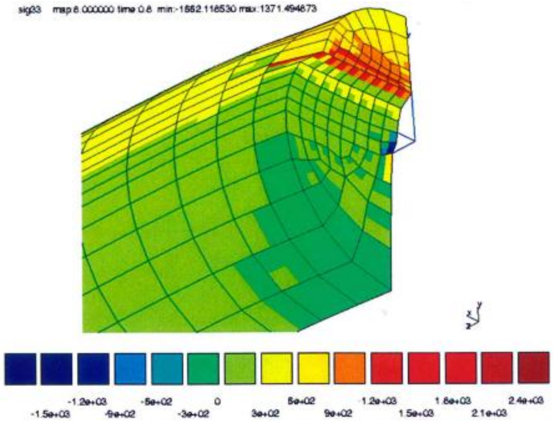

Figure 12. Illustration of a contour maps of the opening stress on a 3D deformed fracture surface for MF1 after FE simulation of propagating crack.

In light of these numerical results, the existence of a ductile cracking regime was confirmed. The calculations revealed a subcritical propagation of the crack up to an optimized value a*, in between the experimental values a_F and a_{max}. A second series of FE computations with a* crack depth was run so as to determine the fracture toughness of the material. The *J-integral* computation was activated during the FE calculation.

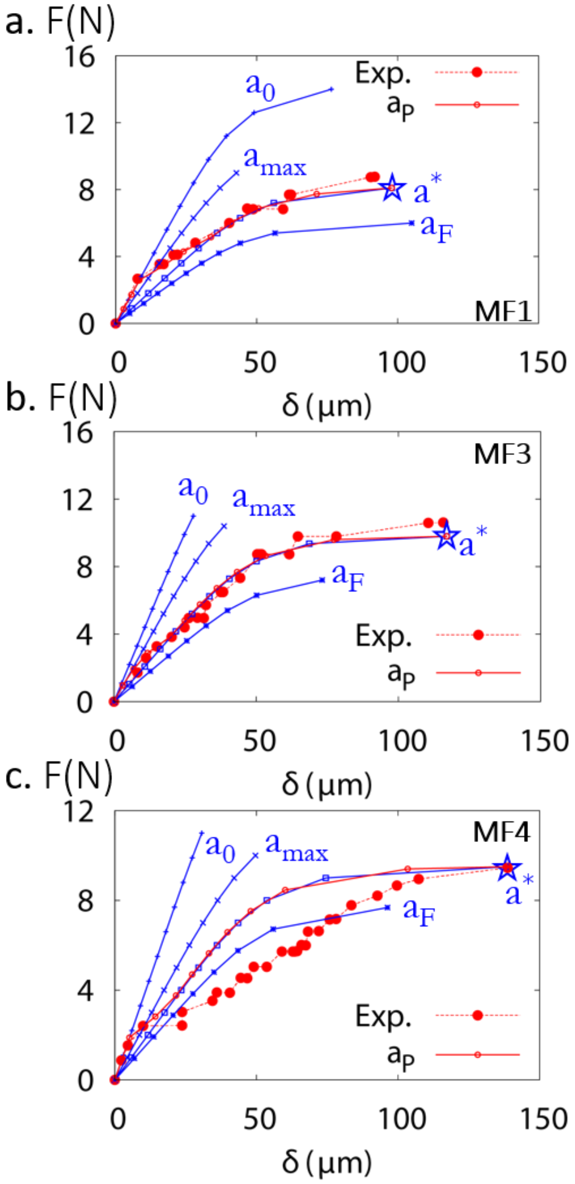

Figure 11. Numerical simulations by compliance analysis and comparison with the experiment (red filled dots) for MF1, MF3 and MF4 geometries. Curves in blue a_0, a_{max} and a_F correspond to stationary cracks, with crack lengths obtained experimentally (see Table 2). Blue curve a* corresponds to a stationary crack for which a* values where optimized by FE computation to be in good accordance with the final compliance. Red curve a_p stands for crack propagation until a*.

The deformed crack surface is shown in Figure 12. J_{IC} was determined by selecting the value of the computed *J-integral* at the maximum load, when the crack depth is supposed to be a*. For each MF fibre, a profile of *J-integral* along the crack front is given in Figure 13, the normalized radius being 0 and 1 at the centre and at the edge of the fibre, respectively.

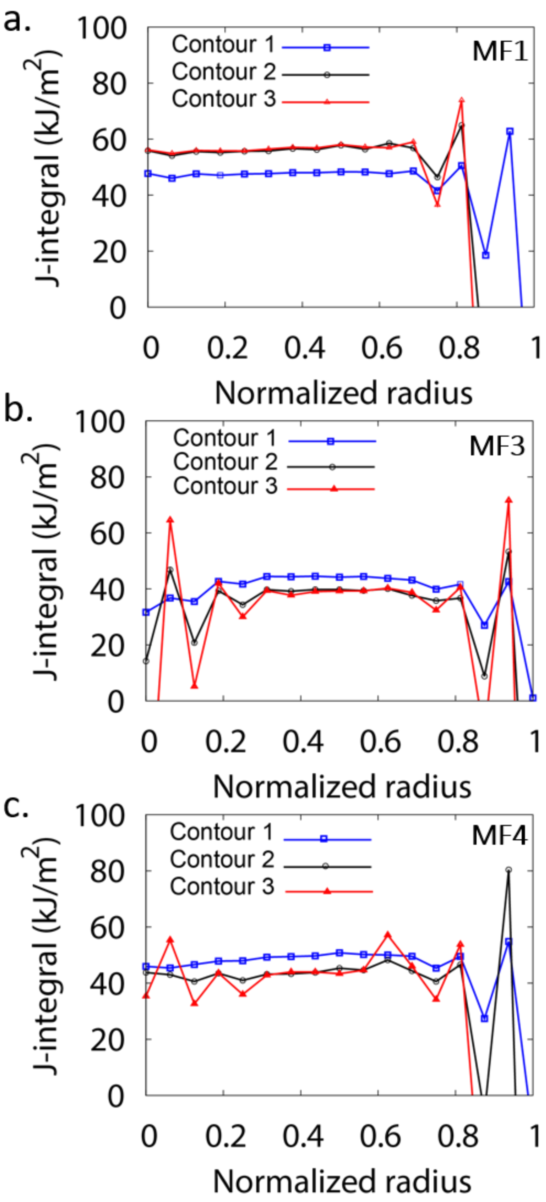

FIGURE 13. Profiles of *J-integral* along the crack fronts for a) MF1, b) MF3 and c) MF4 geometries.

Figure 13 plots the *J-integral* values obtained by FE simulations according to 3 contours around the crack tip node along the crack front.

Although oscillations of the *J-integral* appeared when the element was near a surface, a well-stabilized value of the *J-integral* could be observed elsewhere. This stabilized value was encountered from the second contour of elements around the crack front (Contours 2 and 3). The fracture toughness was taken to be the value of the *J-integral* at the maximum load and corresponded to a* as the crack depth. The average value deduced from Figure 13 was (47 ± 7) kJ.m^{-2}, which is a rather high in comparison with other estimates using linear elastic fracture mechanics (about 15-30 kJ.m^{-2}).[32,36] So as to check the relevance of the *J-integral* computed by FE in fully 3D, the value obtained using experimental curve as suggested by Ramsteiner *et al.*[34] was used:

$$J = \eta\, U_{pl} / (B(\Phi - a)) \qquad (1)$$

where:

- Φ and a are respectively the diameter and the crack depth of the fibre;
- η is a scaling factor, function of a/Φ ;
- U_{pl} is the plastic strain energy corresponding to the area under F-δ curve;
- B is the thickness for plate specimen, here B was assumed to be Φ;

It should be noted that instead of Eq. (1), Michielsen[32] used another formula taken from linear elastic fracture mechanics where the initial crack depth a_0 and the area under the load versus elongation curve (the elongation being L/L_0 and L_0 being the gauge length) were used.

Assuming that at the maximum load, the crack depth had increased to a*, the average value of *J-integral* from Eq. (1) was (46 ± 3) $kJ.m^{-2}$. This value which is very close to that of the FE computation indicates that the η value can be assumed to be the unity. This validates therefore the fracture toughness value obtained by FE simulations.

To go further, Eq. (1) was applied with the same value of U_{pl} but by considering the initial crack depth a_0 instead of a*. Then, the average value of the *J-integral* for MF1 and MF3 was (28 ± 4) $kJ.m^{-2}$. This latter value is closer to that reported by Averett *et al.*[37]. Indeed, Michielsen[32] obtained, for nylon 66 fibre, G_{IC} values ranging from 31.3 kJ m^{-2} to 15.6 kJ m^{-2} respectively for relative humidities of 0% RH and 100% RH. It can concluded that the crack depth value is of prime importance in estimating the fracture toughness of pre-cracked fibre at the microscopic scale.

CONCLUSIONS

A comprehensive investigation of single polyamide 66 fibres was carried out. The experimental data concerning tensile tests consisted of engineering stress-strain curves of three kinds of fibres (UHP, HP and MF). Classical shapes of the engineering stress-strain curves were obtained, the ultimate part exhibiting a plateau assigned to damage mechanisms. The study focused then on this final part of the stress-strain curve obtained in monotonic tensile tests. The fracture surfaces showed two failure zones supposed to be ductile and brittle respectively. The initiation site was systematically on, or very near, the fibre surface.

To better understand the mechanisms of this initiation a test was conducted inside the chamber of the SEM for UHP fibre. A fibre showing two initial defects on the surface was selected. Using a digital camera, side views clearly showed that one of these two defects initiated the degradation of the fibre. The fractography showed the same two surface patterns as encountered on specimens broken after the tensile test. However, a crack propagation by discontinuous bands was also seen on this fracture surface, due to periods of relaxation during the test. As far as authors know this is the first real-time observation of the ductile crack propagation mode in a small diameter polymer fibre.

To go further, four notched fibres with larger diameters were tested *in situ* under an optical microscope. The load was synchronized with the applied displacement, the crack mouth opening displacement, the crack tip opening displacement and the crack advancement were viewed from the side. The load versus crack opening displacement curves were obtained allowing the fracture mechanics theory to be applied. Particular attention was paid to the crack depth measured using side views that were underestimated when compared with that of the *post-mortem* fracture surfaces.

Using the experimental data, FE modelling with crack growth simulation was carried out to fix the crack depth allowing the last brittle failure to occur. Then a stationary crack with this crack depth was used to compute the fracture toughness of the MF fibre. A quite high value of (46 ± 3) $kJ.m^{-2}$ was found compared with other reported values by Michielsen *et al.*[32] (values ranged from 31.3 kJ m^{-2} to 15.6 kJ m^{-2} respectively for relative humidity conditions of 0% RH and 100%). When the calculation was performed with the initial crack depth ratio with the same area under the load versus opening displacement curve, the fracture toughness reduced to (28 ± 4) $kJ.m^{-2}$. This latter value was more in line with the values reported in the literature. This reveals the major challenge of real-time observation of crack propagation mechanisms at the single fibre scale to refine the fracture toughness quantification. In a more general way, this work should contribute to a better understanding of the mechanisms of rupture in complex assemblies as yarns, fabrics or composites.

ACKNOWLEDGEMENTS

The authors acknowledge Gilles Robert for many useful discussions his support. Maria Betbeder and Jean-Christophe Teissedre are acknowledge for their technical help. Authors would thank in memory Yves Favry for his invaluable help throughout many years.

REFERENCES AND NOTES

1. Vollrath, F.; Knight, D. P. Nature **2001**, 410, 541-548.
2. Håkansson, K. M. O.; Fall, A. B.; Lundell, F.; Yu, S.; Krywka, C.; Roth, S. V.; Santoro, G.; Kvick, M.; Prahl Wittberg, L.; Wågberg, L.; Söderberg, L. D. Nature Communications **2014**, 5, 4018.
3. Wollbrett-Blitz, J.; Joannes, S.; Bruant, R.; Le Clerc, C.; De La Osa, M. R.; Bunsell, A.; Marcellan, A. Journal of Polymer Science Part B-Polymer Physics **2016**, 54, 374-384.
4. Laiarinandrasana, L.; Trabelsi, W.; Roirand, Q.; Bunsell, A. R.; Thionnet, A. Applied Composite Materials **2016**, 23, 681-705.
5. Roirand, Q.; Missoum-Benziane, D.; Thionnet, A.; Laiarinandrasana, L. Continuum Mechanics and Thermodynamics **2017**, 29, 1081-1092.
6. Poincloux, S.; Adda-Bedia, M.; Lechenault, F. Physical Review X **2018**, 8.
7. Cheeseman, B. A.; Bogetti, T. A. Composite Structures **2003**, 61, 161-173.
8. Laiarinandrasana, L.; Selles, N.; Klinkova, O.; Morgeneyer, T. F.; Proudhon, H.; Helfen, L. Polymer Testing **2016**, 55, 297-309.
9. Selles, N.; Cloetens, P.; Proudhon, H.; Morgeneyer, T. F.; Klinkoya, O.; Saintier, N.; Laiarinandrasana, L. Macromolecules **2017**, 50, 4372-4383.
10. Marcellan, A.; Bunsell, A. R.; Laiarinandrasana, L.; Piques, R. Polymer **2006**, 47, 367-378.
11. Govaert, L. E.; Peijs, T. Polymer **1995**, 36, 4425-4431.
12. Gonzalez, C.; Llorca, J. Modelling and Simulation in Materials Science and Engineering **2003**, 11, 349-364.
13. Marcellan, A.; Bunsell, A. R.; Piques, R.; Colomban, P. Journal of Materials Science **2003**, 38, 2117-2123.
14. Hearle, J. W. S.; Cross, P. M. Journal of Materials Science **1970**, 5, 507-513.
15. Smook, J.; Hamersma, W.; Pennings, A. J. Journal of Materials Science **1984**, 19, 1359-1373.
16. Hearle, J. W. S.; Lomas, B.; Cooke, W. D. Atlas of Fibre Fracture and Damage to Textiles, Second Edition; Taylor & Francis, **1998**.
17. Bunsell, A. R.; Hearle, J. W. S. Journal of Materials Science **1971**, 6, 1303-1312.
18. Rolland, H.; Saintier, N.; Robert, G. Composites Part B-Engineering **2016**, 90, 365-377.
19. Naito, K.; Yang, J. M.; Tanaka, Y.; Kagawa, Y. Journal of Materials Science **2012**, 47, 632-642.
20. Kant, M.; Penumadu, D. Composites Science and Technology **2013**, 89, 83-88.

21. Ogihara, S.; Imafuku, Y.; Yamamoto, R.; Kogo, Y. Journal of Physics: Conference Series **2009**, 191, 012009.
22. Herraez, M.; Fernandez, A.; Lopes, C. S.; Gonzalez, C. Philosophical Transactions of the Royal Society a-Mathematical Physical and Engineering Sciences **2016**, 374.
23. Ochiai, S.; Kuboshima, S.; Morishita, K.; Okuda, H.; Inoue, T. Journal of the European Ceramic Society **2010**, 30, 1659-1667.
24. Morishita, K.; Ochiai, S.; Okuda, H.; Inshikawa, T.; Sato, M.; Inoue, T. Journal of the American Ceramic Society **2006**, 89, 2571-2576.
25. Feih, S.; Mouritz, A. P.; Case, S. W. Composites Part a-Applied Science and Manufacturing **2015**, 76, 255-261.
26. Prevorsek, D. C.; Coe, A. B.; Lyons, W. J. Textile Research Journal **1965**, 35, 878-898.
27. Bunsell, A. Handbook of Tensile Properties of Textile and Technical Fibres, **2009**.
28. Laiarinandrasana, L.; Kabiri, R. Fatigue & Fracture of Engineering Materials & Structures **2006**, 29, 145-155.
29. Marcellan, A.; Colomban, P.; Bunsell, A. Journal of Raman Spectroscopy **2004**, 35, 308-315.
30. Colomban, P.; Ramirez, J. M. H.; Paquin, R.; Marcellan, A.; Bunsell, A. Engineering Fracture Mechanics **2006**, 73, 2463-2475.
31. Hamouda, H. B. H.; Simaos-betbeder, M.; Grillon, F.; Blouet, P.; Billon, N.; Piques, R. Polymer **2001**, 42, 5425-5437.
32. Michielsen, S. Journal of Materials Science Letters **1992**, 11, 982-984.
33. Toribio, J.; Alvarez, N.; Gonzalez, B.; Matos, J. C. Engineering Failure Analysis **2009**, 16, 794-809.
34. Hale, G.E.; Ramsteiner F. In Fracture Mechanics Testing Methods for Polymers Adhesives and Composites; D.R. Moore, A. Pavan, J.G. Williams (Eds.); ESIS Publication 28. Elsevier, Oxford (UK), **2001**, 123-157
35. Delorenzi, H. G. International Journal of Fracture **1982**, 19, 183-193.
36. Michielsen, S. Journal of Applied Polymer Science **1998**, 67, 1541-1544.
37. Averett, R. D.; Realff, M. L.; Michielsen, S.; Neu, R. W. Composites Science and Technology **2006**, 66, 1671-1681.

GRAPHICAL ABSTRACT

AUTHOR NAMES: Alba Marcellan, Roland Piques, Anthony R. Bunsell, Lucien Laiarinandrasana.

TITLE: *In Situ* Tensile Tests to Analyse the Mechanical Response, Crack Initiation and Crack Propagation in Single Polyamide 66 Fibres.

The study deals with the micro-mechanisms of deformation and failure of single fibres. Crack propagation in single PA66 fibre was observed in the chamber of microscopes. The same tests were performed on fibres with larger diameter containing a controlled notch. The evolution of all measured parameters was followed in real time. Successful numerical simulation on propagating crack was achieved, allowing the failure characteristics of the fibres to be determined.

GRAPHICAL ABSTRACT FIGURE